

Type-II Dirac Photons

Hai-Xiao Wang,^{1,*} Yige Chen,^{2,*} Zhi Hong
Hang,¹ Hae-Young Kee,^{2,3,†} and Jian-Hua Jiang^{1,†}

¹*College of Physics, Optoelectronics and Energy,
& Collaborative Innovation Center of Suzhou Nano Science and Technology,
Soochow University, 1 Shizi Street, Suzhou 215006, China*

²*Department of Physics, University of Toronto, Toronto, M5S 1A7, Canada*

³*Canadian Institute for Advanced Research,
Toronto, Ontario, M5G 1Z8, Canada*

(Dated: April 6, 2017)

* These authors contributed equally

† Correspondence should be addressed to: jianhua.jiang.phys@gmail.com or hykee@physics.utoronto.ca

The Dirac equation for relativistic electron waves is the parent model for Weyl and Majorana fermions as well as topological insulators. Simulation of Dirac physics and band topology in three-dimensional time-reversal invariant photonic systems, though fundamentally important for topological phenomena at optical frequencies, encounters the challenge of synthesis of both Kramers double degeneracy and parity inversion. Here we show how type-II Dirac points—exotic Dirac relativistic waves yet to be discovered—are robustly realized through screw symmetry. The emergent type-II Dirac points carry nontrivial topology and are the mother states of type-II Weyl points. The proposed all-dielectric photonic-crystal architecture allows unprecedented control of electromagnetic waves, including robust “open-cavity” states at photonic-crystal—air interfaces and anomalous refraction, with low energy dissipation.

Dirac’s famous equation for relativistic electron waves[1] is the foundation for both the quantum field theory and the later topological insulators and semimetals[2–5]. There has been a trend in the simulation of relativistic waves and topological states in classical dynamics such as electromagnetic[6, 7], acoustic[8–11] and mechanical waves[12, 13], mostly in 2D systems. Many unprecedented phenomena in electromagnetics are discovered along this paradigm, such as photonic *Zitterbewegung*[14] and pseudodiffusion[15], dielectric zero-index metamaterials[16], deformation induced pseudomagnetic field and photonic Landau levels[17], Klein tunneling and supercollimation of photons[18], and photonic topological insulators and semimetals with[19–23] and without[6, 24–27] time-reversal (\mathcal{T}) symmetry. Recently, such simulation develops from 2D to 3D[28–35], exposing to larger configuration and wavevector spaces that may lead to rich physical phenomena and applications, particularly in \mathcal{T} -invariant photonic systems which are more feasible for high-frequency (e.g., infrared or visible) applications.

The fundamental challenges in the simulation of the Dirac equation in classical waves are the *synthesis* of both fermionic Kramers degeneracy and parity inversion with additional symmetries (totaling fourfold degeneracy), since in bosonic systems $\mathcal{T}^2 = 1$ and the time-reversal symmetry does *not* guarantee double degeneracy. Although there have been a few delicate designs[32, 34, 35], an effective methodology for the simulation of Dirac relativistic

physics in classical waves is still lack. In photonic crystals (PhCs) with C_6 symmetry, there are two types of doublets with opposite parities that enable the simulation of Dirac points (DPs) in 2D[10, 19, 23] and 3D[32, 35]. Outside the point-group symmetry, glide symmetry was exploited to realize 3D DPs[34]. However, both the C_6 point-group symmetry and the glide symmetry can only lead to Kramers degeneracy at certain high symmetry *lines* in the Brillouin zone (BZ). In addition, the C_6 point-group does not guarantee double degeneracy for all photonic bands on the high-symmetry line. There are other nondegenerate bands which can mess up the spectrum[32]. Moreover, only type-I DPs have been studied up till now. The concept of type-II DPs, as analog of the type-II Weyl points (WPs) but with fourfold degeneracy instead of twofold[36, 37], though studied very recently in electronic theories[38], has never been discovered in photonic and other bosonic systems.

The distinction between symmorphic (e.g., point-group) and nonsymmorphic spatial symmetries in crystals lies in whether the spatial origin can be preserved. Nonsymmorphic symmetries cannot preserve the spatial origin but translate it by a fraction of the crystal period. It is known that such translation can introduce unconventional mechanisms for band degeneracy[39, 40]. An elementary type of nonsymmorphic symmetry, beside the glide symmetry, is the screw symmetry: a rotation accompanied with a fraction of lattice translation. So far, the role of screw symmetry on the realization of topological states in classical/bosonic waves has not yet been explored. Here we unveil that screw symmetries can lead to Kramers double degeneracy for *all* Bloch states on certain *planes* in the BZ, thus creating a very large wavevector space for the simulation of DPs and the Z_2 topology. The screw symmetries become particularly powerful when there are two orthogonal screw axes, since the product of the two screw rotations is essentially the parity that protects the DPs. Thus the two screw symmetries can simultaneously synthesize both elements of DPs: the fermionic Kramers degeneracy (“spin”) and parity (“orbit”) inversion. In comparison, to simulate DPs using a glide symmetry, two additional mirror or glide symmetries are needed to create the parity (“orbit”) degree of freedom. Our symmetry-guided approach provides a robust paradigm toward DPs and the Z_2 topology in \mathcal{T} -invariant bosonic systems, without relying on fine-tuning or sophisticated design. Exploiting this paradigm, we demonstrate that both type-II and type-I DPs with nontrivial Z_2 topology can be realized in tetragonal all-dielectric PhCs. The non-chiral topological surface states induced by the DPs are found below the light-line and form resilient “open-cavity” states on the PhC-air

interfaces. By reducing the space symmetry, type-II Weyl points (WPs) are derived from DPs. Abnormal refraction with one or two pairs of opposite refraction angles is uncovered for type-II DPs/WPs. To the best of our knowledge, this is the first discovery of type-II DPs in photonics and the first proposal of type-II WPs in *all-dielectric* PhCs. Our findings may enable unprecedented control of light at optical frequencies with low dissipation.

Results

All-dielectric photonic-crystal architecture

To be concrete, we consider a simple design of all-dielectric PhC of tetragonal lattice with space group of $P4_2/mcm$, although our approach can also be applied for other classical/bosonic waves. The PhC structure is schematically illustrated in Figs. 1a and 1b. In each unit cell (with lattice constant $a \equiv 1$ along all three directions) there are two orthogonal dielectric blocks (painted as yellow and green in Fig. 1, respectively) of the same shape and permittivity ε_b which are embedded in a polymer matrix of permittivity ε_m . We shall first set the length l , width w and height h of the blocks as $l = 0.5$, $w = 0.2$, and $h = 0.5$. The permittivities are set as $\varepsilon_b = 16$ (germanium) and $\varepsilon_m = 1.9$ (polymers). We show later that DPs also emerge for other material/geometric parameters, revealing the robustness and effectiveness of our symmetry-guided approach. These PhCs can in principle be fabricated using layer-by-layer methods with the current technology[41, 42] for infrared frequencies. We use the MIT PHOTONIC BANDS[43] to calculate the photonic spectrum for the bulk bands in the BZ and the surface bands in the surface BZ (see the inset of Fig. 1c).

The tetragonal symmetries crucial to our study are the two-fold screw symmetries $S_x := (x, y, z) \rightarrow (\frac{1}{2} + x, \frac{1}{2} - y, \frac{1}{2} - z)$ and $S_y := (x, y, z) \rightarrow (\frac{1}{2} - x, \frac{1}{2} + y, \frac{1}{2} - z)$ (illustrated in Fig. 1b). The 180° rotation around the z axis, $C_2 := (x, y, z) \rightarrow (-x, -y, z)$, is important as well. Other relevant symmetries include the inversion symmetry $\mathcal{P} := (x, y, z) \rightarrow (-x, -y, -z)$, the time-reversal symmetry $\mathcal{T} : t \rightarrow -t$, and the mirror symmetries $M_1 := (x, y, z) \rightarrow (y, x, z)$, $M_2 := (x, y, z) \rightarrow (-y, -x, z)$, and $M_z := (x, y, z) \rightarrow (x, y, -z)$. The remaining symmetries are listed and analyzed in the Supplementary Materials. The nonsymmorphic symmetries transform the yellow blocks into green blocks (and vice versa), while the point-group symmetries transform within each color, as illustrated in Fig. 1b.

Photonic Kramers degeneracy

To elucidate the effect of screw symmetries, we construct the following *anti-unitary* operators: $\Theta_i \equiv S_i * \mathcal{T}$ ($i = x, y$). The time-reversal operation \mathcal{T} is manifested as the complex conjugation of the photonic “wavefunction” for a Bloch state $\Psi_{n\vec{k}}(\vec{r}) = (\vec{e}_{n\vec{k}}, \vec{h}_{n\vec{k}})^T$ (here \vec{e} and \vec{h} are the electric and magnetic fields of the photon, respectively) with additional sign reversal for the magnetic fields. Since $\Theta_x^2 = S_x^2 = T_{100}$ where T_{100} is a spatial translation by the coordinate vector $\vec{r} = (1, 0, 0)$, acting Θ_x twice on a photonic Bloch state $\Psi_{n\vec{k}}(\vec{r})$ gives $\Theta_x^2 \Psi_{n\vec{k}}(\vec{r}) = e^{ik_x} \Psi_{n\vec{k}}(\vec{r})$ (see details in Methods). Θ_x transforms (k_x, k_y, k_z) into $(-k_x, k_y, k_z)$ and is hence an invariant operation on the $k_x = \pi$ plane where we find

$$\Theta_x^2 = e^{ik_x} \Big|_{k_x=\pi} = -1. \quad (1)$$

Following the same argument of the Kramers theorem, *all* Bloch states on the *whole* $k_x = \pi$ plane are doubly degenerate (see Fig. 1c). The above relation is crucial for the synthesis of fermionic Kramers degeneracy in bosonic systems. Similarly, all Bloch states are doubly degenerate on the whole $k_y = \pi$ plane, due to $\Theta_y^2 = -1$.

Dirac Points

The synthetic “Kramers” double degeneracy on the two BZ boundary planes create a very large wavevector space for the simulation of Dirac physics and Z_2 topology. The next important step is to realize parity-inversion. The parity can be defined through the C_2 rotation around the z axis, which is invariant on the MA and XR lines. The product of the two orthogonal screw rotations yields exactly C_2 : $S_y S_x = T_{010} C_2$ and $S_x S_y = T_{100} C_2$. Therefore on the MA line one has $\Theta_y \Theta_x = \Theta_x \Theta_y = -C_2$, i.e., the Θ_x operator *commutes* with both Θ_y and C_2 on the MA line. Elegantly, the above algebra reveals that the two degenerate states in any doublet have the *same* eigenvalue of the C_2 operator. Such eigenvalues $c_2 = \pm 1$ precisely represent the parities of the photonic states in the x - y plane. Crossing between two doublets with opposite parities on the MA line leads to a 3D DP. According to Ref. [44], the topological charge of the DP is a measure of parity-inversion, $\mathcal{N}_{DP} = \frac{1}{2} [c_2^-(k_0^+) - c_2^-(k_0^-)]$, where c_2^- is the parity of the lower branch of the Dirac cone, and $k_0^+ = k_0 + 0^+$ ($k_0^- = k_0 - 0^+$) is the wavevector slightly larger (smaller) than the wavevector of the DP on the z direction, k_0 . Hence a DP is essentially a source or sink of parity-inversion in photonic bands. Fig. 1d shows that there are four DPs in the first six bands with topological charges $\mathcal{N}_{DP} = \pm 1$, due to the crossing between the doubly degenerate p -wave and d -wave states (see Fig. 1d

for field profiles).

Remarkably, we find that our symmetry-oriented paradigm provides a robust and effective approach toward Z_2 topological DPs: Fig. 1e shows that the emergence of DPs is quite robust to the shape and permittivity of the dielectric blocks (more examples are given in the Supplementary Materials), since any crossing between bands of different parities can lead to DPs.

The spin-orbit physics of the Dirac points can be understood via a symmetry-based $\vec{k} \cdot \vec{P}$ theory (see Supplementary Materials for details). The Hamiltonian can be constructed using the basis of the two doublets p_1 and p_2 , d_1 and d_2 [Fig. 1d]. Recombination of these states gives $|p_{\pm}\rangle = \frac{1}{\sqrt{2}}(|p_1\rangle \pm i|p_2\rangle)$ and $|d_{\pm}\rangle = \frac{1}{\sqrt{2}}(|d_1\rangle \pm i|d_2\rangle)$, which carry total angular momenta (TAM) that are opposite for the $+$ and $-$ states (see Supplementary Materials). Emulating fermionic spin and orbit with TAM and parity, respectively, we find the following photonic Hamiltonian for a DP,

$$\hat{\mathcal{H}} = \omega_0 + v \begin{pmatrix} (\eta + 1)q_z \hat{1} & \hat{\mathcal{A}} \\ \hat{\mathcal{A}}^\dagger & (\eta - 1)q_z \hat{1} \end{pmatrix} + \mathcal{O}(q^2), \quad \hat{\mathcal{A}} \equiv \vec{g} \cdot \hat{\vec{\sigma}}. \quad (2)$$

where ω_0 is the frequency of the DP, v is the characteristic group velocity, $\hat{1}$ is the 2×2 identity matrix, $\hat{\vec{\sigma}}$ is the Pauli matrix vector, $g_x = \alpha q_2 - \alpha^* q_1$, $g_y = \beta q_1 - \beta^* q_2$, $g_z = i(\beta q_1 + \beta^* q_2)$, $q_1 = \frac{q_x + q_y}{\sqrt{2}}$, $q_2 = \frac{-q_x + q_y}{\sqrt{2}}$, $\vec{q} \equiv \vec{k} - (\pi, \pi, k_0)$, α and β are the (complex) $\vec{k} \cdot \vec{P}$ coefficients, and $\mathcal{O}(q^2)$ denotes the quadratic warping (and higher-order) terms. Here the spin-orbit coupling is emulated by the k -linear interaction between the p and d bands which originates from the magneto-electric coupling in the Maxwell equations. The above Hamiltonian describes a generalized massless 3D Dirac relativistic wave, differing from other Dirac waves known so far[19, 32, 34, 35]. The 3D Dirac wave can also be regarded as a series of q_z -dependent 2D Dirac waves of which the Dirac mass, $m_D \equiv vq_z$, can be positive, negative (i.e., parity-inversion), or zero.

Derived type-II and type-I Weyl Points

A DP can be regarded as composed of a pair of WPs of opposite Chern numbers. Thus when the space symmetry is reduced WPs can emerge from DPs[32]. To realize the WPs, we deform the unit-cell structure in such a way (as displayed in Fig. 2a) that the two screw symmetries S_x and S_y , the three mirror symmetries M_1 , M_2 and M_z , as well as the inversion

symmetry \mathcal{P} are broken. However, the C_2 symmetry is still preserved. The removal of the two screw symmetries lifts the deterministic double degeneracy on the MA line. However, accidental degeneracy between bands of opposite parity is protected by the C_2 symmetry. The chiral structure of the PhC results in p_{\pm} - and d_{\pm} -like states in the photonic bands. The crossings between the p and d bands results in WPs of Chern number ± 1 (see Supplementary Materials for a $\vec{k} \cdot \vec{P}$ analysis). We identify six WPs in Fig. 2b (there are more WPs in higher frequency regions, explaining the nonzero total Chern number). Fig. 2b also shows that there are four type-II WPs and two type-I WPs. The 3D dispersions of both type-I and type-II WPs on the lowest d -band are shown in Fig. 2c. Our proposal of all-dielectric-PhC realization of type-II WPs allows realization of lossless type-II WPs.

Robust surface states

According to the bulk-edge correspondence principle[2–5], the (100) surface states of the tetragonal PhC can reveal the Z_2 topology of the DPs. We then calculate the surface and projected bulk photonic spectrum using a supercell stacking along the x direction [see Methods]. Fig. 3a shows a gapless surface band traversing the projected photonic band gap. This surface band is between the upper and lower branches of the type-I DP, but above both branches of the type-II DP. Thus the gapless surface band is induced by the type-I topological DPs. Nevertheless, both type-I and type-II DPs have the same Z_2 topology (see Fig. 1). The topological surface states carry finite TAM as indicated in Fig. 3b by the winding of the Poynting vectors. The photonic TAM reverse sign when the wavevector reverse sign (see Fig. 3b). This property is similar to the spin-wavevector locking on the edge of topological insulators[2, 3]. We find that the two symmetries, S_y and \mathcal{T} , guarantee that the spectrum in the surface BZ is symmetric under the transformation $(k_y, k_z) \rightarrow (\pm k_y, \pm k_z)$ (see Methods). Such a non-chiral surface band of our PhC, distinctive from the chiral surface states due to Weyl points[28, 30, 31], has never been found in photonics before. Remarkably, here the topological surface states are below the light-line and form “open-cavity” states on the PhC-air interfaces without additional cladding.

The robustness of the topological surface states can be revealed via their frequency stability against surface modifications. Fig. 3c shows that the frequency of the topological surface state is quite robust and insensitive to variations of the thickness of a dielectric slab placed on top of the PhC surface. The change of frequency is within 2.5%, although the field

profile has been substantially modified (see Fig. 3d). Comparison between the topological surface state and the slab-defect state in a typical sandwich-structure with woodpile-PhC cladding[46] (see inset of Fig. 3c and details in Methods) shows that the topological surface state is more robust, even though there is no complete photonic band gap in the tetragonal PhC (while the woodpile PhC has a large complete photonic band gap of $\delta\omega/\omega = 21\%$). These topological surface states thus form resilient, subwavelength-confined quasi-2D photonic systems. The nontrivial topology/Berry-phases and the gapless spectrum distinct the topological surface states from conventional PhC surface states[47].

Spectral and optical properties

There are two types of DPs, which in analog of type-I and type-II WPs[36, 37], are termed as type-I and type-II DPs (both of them appear in Fig. 1d). From Eq. (2), the photonic spectrum around a DP in the k_x - k_z plane (Fig. 4a) is

$$\omega = \omega_0 + v\eta q_z + v\tau\sqrt{q_z^2 + \gamma^2 q_x^2}, \quad (3)$$

where $\tau = \pm$ stands for the upper and lower branches of the DP, respectively, the dimensionless parameters $\gamma = \frac{1}{\sqrt{2}}\sqrt{|\alpha|^2 + |\beta|^2}$ and η measure the deformation of the Dirac cone. The classification of type-I and type-II DPs here depends on the parameter η : $|\eta| > 1$ for type-II DPs and $|\eta| < 1$ for type-I DPs. The isofrequency contour near a type-II DP is a hyperbolic curve (Fig. 4b). In contrast, the isofrequency contours near a type-I DP is of elliptical shapes. When $\omega = \omega_0$, the two branches touch each other and the isofrequency contour becomes a pair of crossing lines (Fig. 4c), between which the angle is $\theta_{DP} = 2 \arctan\left(\sqrt{\frac{\eta^2-1}{\gamma^2}}\right)$. A finite angle θ_{DP} signals the type-II DPs. The classification of type-I and type-II DPs does not affect the topological charge: both type-I and type-II DPs can have the same topological charge (see Fig. 1d).

The dispersion of the type-II DP in the k_x - k_y plane is distinctive from the existing DPs[19, 32, 34, 35] (see Fig. 4d). This spectrum can be understood via the $\vec{k} \cdot \vec{P}$ Hamiltonian (2) which yields $\omega_{\tau,i}(\vec{q}) = \omega_0 + v\eta q_z + v\tau\sqrt{q_z^2 + 2\gamma^2|q_i|^2} + \mathcal{O}(q^2)$, with $\tau = \pm$ and $i = 1, 2$. This spectrum is nondegenerate for finite q_x and q_y . The two-fold degeneracy is restored only on the $k_x = \pi$ and the $k_y = \pi$ planes (i.e., when $q_x = 0$ or $q_y = 0$) by the screw symmetries, recovering the dispersion in Eq. (3). Such V-shaped dispersion gives elliptical-shaped isofrequency contours or non-closing contours in the k_x - k_y plane (Figs. 4e and 4f),

depending on the quadratic warping terms.

Along with the unique photonic spectrum, it is found that the type-II DPs host anomalous refraction of light: as schematically depicted in Fig. 4g, there are two refraction beams of opposite angles, if the incident beam is in the x - z (or y - z) plane. We consider a light beam injected from a medium with large refraction index $n_i > 1.65$ to enable frequency and wavevector matching with the Dirac cone. The refraction angle is determined through the group velocities in the PhC as, $\theta_r \equiv -\arctan(\frac{v_x}{v_z})$. Using the dispersion in Eq. (3), we find that $v_z = v \left(\eta + \frac{\tau q_z}{\sqrt{\gamma^2 q_x^2 + q_z^2}} \right)$, $v_x = \frac{\tau v \gamma q_x}{\sqrt{\gamma^2 q_x^2 + q_z^2}}$. Interestingly, as only the solutions with negative v_z deliver the refraction beams, one readily finds that for $\eta > 1$, there is no refraction. In contrast, for $\eta < -1$, there are two refraction beams of opposite refraction angles, as depicted in Fig. 4c, with

$$\theta_{r2} = -\theta_{r1}. \quad (4)$$

Since the two DPs at opposite \vec{k} 's, which can also be regarded as two “valleys”[11], have opposite η , the above property then allows *valley-selective* excitation of type-II DPs.

An intuitive interpretation of Eq. (4) can be drawn from the group velocity profiles in Figs. 4b and 4c: the group velocities for the upper and lower branches are always directed to two opposite direction with respect to the k_z axis. An analytic proof of such a property is presented in the Methods section, which is confirmed in Fig. 4h for various frequencies and parameters. Away from the $k_x = \pi$ and $k_y = \pi$ planes, the photonic spectrum is nondegenerate, leading to two pairs of refraction beams with opposite angles, as shown in Fig. 4i where the angle of incidence $\phi_i = \text{Arg}(q_x + iq_y)$ is varied. Zero refraction angle is realized when ϕ_i is close to $\frac{\pi}{4}$, $\frac{3\pi}{4}$, $\frac{5\pi}{4}$, or $\frac{7\pi}{4}$, due to vanishing group velocity in the k_x - k_y plane. The above unconventional optical properties also holds for type-II WPs. However, as WPs are two-fold degenerate, there are only two refraction beams. Coexisting positive and negative refraction was found in a 2D model system before[45]. Our study establishes concurrent negative and positive refraction for 3D all-dielectric PhCs, which may enable simultaneous real and virtual imaging.

Discussions

The band topology induced by crystalline symmetries are in the context of topological crystalline states[49, 50]. Weak disorders that preserve the crystalline symmetry on average

do not destroy the topological orders and surface states[32, 50]. Using crude spatial meshes [with mesh size as large as $(0.125a)^3$ compared to the dielectric block size $(0.368a)^3$] in the photonic bands calculation as a method of mimicking disorders, we find that both the DPs and the topological surface states are quite robust to disorders (see Supplementary materials for details). In fact, such simulation shows that the DPs in our PhC are even more robust than the WPs found in Ref. [28] where the parity breaking perturbation $\lesssim (0.1a)^3$ can substantially modify the number of WPs. The resilient topological states in our system provide unprecedented opportunities for optoelectronic devices on the PhC-air interfaces, which are easier to fabricate, manipulate, and probe (e.g., using near-field scanning spectroscopy), compared to conventional cavities and waveguides embedded in PhCs[48]. Our all-dielectric topological PhC architecture may inspire discovery of other 3D topological photonic states in all-dielectric photonics, and stimulate future synergy between subwavelength photonic topological metamaterials and optoelectronics on the PhC surfaces.

Methods

Symmetry transformation of the photonic states

A photonic state $\Psi_{n\vec{k}}(\vec{r})$ transforms under the $\Theta_x = S_x * \mathcal{T}$ operation as follows,

$$\Theta_x \Psi_{n\vec{k}}(\vec{r}) = \hat{m}_y \hat{m}_z \hat{t}_h \Psi_{n\vec{k}}^*(S_x \vec{r}), \quad (5)$$

where \hat{m}_y and \hat{m}_z are the mirror transformation for the electric and magnetic fields:

$$\hat{m}_y E_i = \bar{\delta}_{iy} E_i, \quad \hat{m}_y H_i = -\bar{\delta}_{iy} H_i, \quad i = x, y, z, \quad (6)$$

$$\bar{\delta}_{ij} = \begin{cases} 1, & \text{if } i \neq j \\ -1, & \text{if } i = j \end{cases}, \quad (7)$$

and the operator \hat{t}_h reverses the sign of the magnetic field. Acting Θ_x twice yields,

$$\Theta_x^2 \Psi_{n\vec{k}}(\vec{r}) = \Psi_{n\vec{k}}(S_x^2 \vec{r}) = \Psi_{n\vec{k}}(T_{100} \vec{r}) = e^{ik_x} \Psi_{n\vec{k}}(\vec{r}). \quad (8)$$

Refraction

The photonic dispersion in the medium with refraction index n_i is given by $\omega = c|\vec{k}|/n_i$. Around the DP at $\vec{K}_0 = (\pi, \pi, k_0)$, the dispersion in the medium can be expressed as

$\omega = c|\vec{k}|/n_i = c|\vec{K}_0 + \vec{q}|/n_i$ where $\vec{q} = \vec{k} - \vec{K}_0$. Since the perpendicular wavevector k_z is not conserved during refraction, we can always set

$$q_x = q_{\parallel} \cos(\phi_i), \quad q_y = q_{\parallel} \sin(\phi_i) \quad (9)$$

for fixed q_{\parallel} , while adjusting k_z to keep a constant frequency. The angle ϕ_i is varied from 0 to 2π . The refraction in the x - z plane is determined by matching the frequency and the parallel wavevector, yielding

$$\omega - \omega_0 = v(\eta q_z + \tau \sqrt{q_z^2 + \gamma^2 q_x^2}), \quad \tau = \pm 1. \quad (10)$$

The perpendicular wavevector q_z in the PhC is determined by the above equation, which has two solutions for $\eta < -1$

$$q_z^{\tau} = \frac{\eta(\omega - \omega_0) + \tau \sqrt{(\omega - \omega_0)^2 + v^2(\eta^2 - 1)\gamma^2 q_x^2}}{v(\eta^2 - 1)}. \quad (11)$$

Inserting this into the definition of the refraction angle, we obtain

$$\theta_{r2} = -\theta_{r1} = -\arctan \left(\frac{v\gamma q_x}{\sqrt{(\omega - \omega_0)^2 + v^2(\eta^2 - 1)\gamma^2 q_x^2}} \right). \quad (12)$$

Refraction for generic \vec{q} (i.e., away from the x - z or y - z plane) is given in details in the Supplementary Materials.

Calculation of surface states

The surface states are obtained by supercell calculations. The supercell is periodic in the y - z plane but finite in the x direction. There are seven layers of unit cell along this direction as sandwiched by air layers of length $3a$ on the left and right, separately. The simple cladding medium (air) used here is non-topological for all polarizations and useful to study topological surface states below the light-line. The supercell structure is set to preserve the S_y symmetry. Since S_y transforms $\vec{k} = (k_y, k_z)$ to $(k_y, -k_z)$ in the surface BZ, the surface spectrum is symmetric with respect to $k_z = 0$ and $k_z = \pi$. In addition, the \mathcal{T} symmetry guarantees that the surface spectrum is invariant under the transformation $\vec{k} = (k_y, k_z)$ to $(-k_y, -k_z)$. Therefore the surface photonic dispersion is also symmetric with respect to $k_y = 0$ and $k_y = \pi$.

In the calculation of the reference slab-defect states, we have set the permittivity of the slab-defect layer as $\varepsilon = 8$ (the same as that of the dielectric slab on top of the topological

PhC). The logs of the woodpile PhCs above and below the slab-defect layer are of width $0.25a$, height $0.3a$ and permittivity of 12 (silicon).

References

- [1] P. A. M. Dirac, *The quantum theory of the electron*, Proc. Roy. Soc. A (London) **117**, 610624. (1928).
- [2] M. Z. Hasan and C. L. Kane, *Topological insulators*, Rev. Mod. Phys. **82**, 3045-3067 (2010).
- [3] X.-L. Qi and S.-C. Zhang, *Topological insulators and superconductors*, Rev. Mod. Phys. **83**, 1057-1110 (2011).
- [4] O. Vafek and A. Vishwanath, *Dirac fermions in solids: from high- T_c cuprates and graphene to topological insulators and Weyl semimetals*, Ann. Rev. Cond. Matt. Phys. **5**, 83-112 (2014).
- [5] Y. Chen, Y.-M. Lu, and H.-Y. Kee, *Topological crystalline metal in orthorhombic perovskite iridates*, Nat. Commun. **6**, 6593 (2015).
- [6] F. D. M. Haldane and S. Raghu, *Possible realization of directional optical waveguides in photonic crystals with broken time-reversal symmetry*, Phys. Rev. Lett. **100**, 013904 (2008).
- [7] L. Lu, J. D. Joannopoulos, and M. Soljačić, *Topological photonics*, Nat. Photon. **8**, 821 (2014).
- [8] Z. Yang, F. Gao, X. Shi, X. Lin, Z. Gao, Y. Chong, and B. Zhang, *Topological acoustics*, Phys. Rev. Lett. **114**, 114301 (2015).
- [9] M. Xiao, W.-J. Chen, W.-Y. He, and C. T. Chan, *Synthetic gauge flux and Weyl points in acoustic systems*, Nat. Phys. **11**, 920924 (2015).
- [10] C. He, X. Ni, H. Ge, X.-C. Sun, Y.-B. Chen, M.-H. Lu, X.-P. Liu, and Y.-F. Chen, *Acoustic topological insulator and robust one-way sound transport*, Nat. Phys. **12**, 11241129 (2016).
- [11] J. Lu, C. Qiu, M. Ke, and Z. Liu, *Valley vortex states in sonic crystals*, Phys. Rev. Lett. **116**, 093901 (2016).
- [12] R. Süssstrunk and S. D. Huber, *Observation of phononic helical edge states in a mechanical topological insulator*, Science **349**, 4750 (2015).
- [13] D. Z. Rocklin, B. G.-g. Chen, M. Falk, V. Vitelli, and T.C. Lubensky, *Mechanical Weyl modes in topological Maxwell lattices*, Phys. Rev. Lett. **116**, 135503 (2016).

- [14] X. Zhang, *Observing Zitterbewegung for photons near the Dirac point of a two-dimensional photonic crystal*, Phys. Rev. Lett. **100**, 113903 (2008).
- [15] R. A. Sepkhanov, Ya. B. Bazaliy, and C. W. J. Beenakker, *Extremal transmission at the Dirac point of a photonic band structure*, Phys. Rev. A **75**, 063813 (2007).
- [16] X. Q. Huang, Y. Lai, Z. H. Hang, H. H. Zheng, and C. T. Chan, *Dirac cones induced by accidental degeneracy in photonic crystals and zero-refractive-index materials*, Nat. Mater. **10**, 582-586 (2011).
- [17] M. C. Rechtsman, J. M. Zeuner, A. Tünnermann, S. Nolte, and M. Segev, and A. Szameit, *Strain-induced pseudomagnetic field and photonic Landau levels in dielectric structures*, Nat. Photon. **7**, 153-158 (2013).
- [18] A. Fang, Z. Q. Zhang, S. G. Louie, and C. T. Chan, *Klein tunneling and supercollimation of pseudospin-1 electromagnetic waves*, Phys. Rev. B **93**, 035422 (2016).
- [19] K. Sakoda, *Dirac cone in two- and three-dimensional metamaterials*, Opt. Express **20**, 3898-3917 (2012).
- [20] A. B. Khanikaev, S. H. Mousavi, W.-K. Tse, M. Kargarian, A. H. MacDonald, and G. Shvets, *Photonic topological insulators*, Nat. Mater. **12**, 233 (2013).
- [21] W.-J. Chen, S.-J. Jiang, X.-D. Chen, J.-W. Dong, and C. T. Chan, *Experimental realization of photonic topological insulator in a uniaxial metacrystal waveguide*, Nat. Commun. **5**, 5782 (2014).
- [22] T. Ma, A. B. Khanikaev, S. H. Mousavi, and G. Shvets, *Guiding electromagnetic waves around sharp corners: topologically protected photonic transport in metawaveguides*, Phys. Rev. Lett. **114**, 127401 (2015).
- [23] L.-H. Wu and X. Hu, *Scheme for achieving a topological photonic crystal by using dielectric material*, Phys. Rev. Lett. **114**, 223901 (2015).
- [24] Z. Wang, Y. Chong, J. D. Joannopoulos, and M. Soljačić, *Observation of unidirectional backscattering-immune topological electromagnetic states*, Nature (London) **461**, 772-775 (2009).
- [25] M. Hafezi, S. Mittal, J. Fan, A. Migdall, and J. Taylor, *Imaging topological edge states in silicon photonics*, Nat. Photon. **7**, 1001 (2013).
- [26] M. C. Rechtsman, J. M. Zeuner, Y. Plotnik, Y. Lumer, D. Podolsky, F. Dreisow, S. Nolte, M. Segev, and A. Szameit, *Photonic Floquet topological insulators*, Nature **496**, 196 (2013).

- [27] S. Mittal, S. Ganeshan, J. Fan, A. Vaezi, and M. Hafezi, *Measurement of topological invariants in a 2D photonic system*, Nat. Photon. **10**, 180 (2016).
- [28] L. Lu, L. Fu, J. D. Joannopoulos, and M. Soljačić, *Weyl points and line nodes in gyroid photonic crystals*, Nat. Photon. **7**, 294 (2013).
- [29] L. Lu, Z. Wang, D. Ye, L. Ran, L. Fu, J. D. Joannopoulos, and M. Soljačić, *Experimental observation of Weyl points*, Science **349**, 622 (2015).
- [30] W. Gao, B. Yang, M. Lawrence, F. Fang, B. Béri, and S. Zhang, *Plasmon Weyl degeneracies in magnetized plasma*, Nat. Comm. **7**, 12435 (2016).
- [31] W.-J. Chen, M. Xiao, and C. T. Chan, *Experimental observation of robust surface states on photonic crystals possessing single and double Weyl points*, Nat. Commun. **7**, 13038 (2016).
- [32] H.-X. Wang, L. Xu, H.Y. Chen, and J.-H. Jiang, *Three-dimensional photonic Dirac points stabilized by point group symmetry*, Phys. Rev. B **93**, 235155 (2016).
- [33] M. Xiao, Q. Lin, and S. Fan, *Hyperbolic Weyl point in reciprocal chiral metamaterials*, Phys. Rev. Lett. **117**, 057401 (2016).
- [34] L. Lu, C. Fang, L. Fu, S. G. Johnson, J. D. Joannopoulos, and M. Soljačić, *Symmetry-protected topological photonic crystal in three dimensions*, Nat. Phys. **12**, 337 (2016).
- [35] A. Slobozhanyuk, S. H. Mousavi, X. Ni, D. Smirnova, Y. S. Kivshar, and A. B. Khanikaev, *Three-dimensional all-dielectric photonic topological insulator*, Nat. Photon. **11**, 130136 (2017).
- [36] A. A. Soluyanov, D. Gresch, Z. Wang, Q. Wu, M. Troyer, X. Dai, and B. A. Bernevig, *Type-II Weyl semimetals*, Nature (London) **527**, 495-498 (2015).
- [37] Yong Xu, Fan Zhang, and Chuanwei Zhang, Phys. Rev. Lett. **115**, 265304 (2015).
- [38] H. Huang, S. Zhou, and W. Duan, *Type-II Dirac fermions in the PtSe₂ class of transition metal dichalcogenides*, Phys. Rev. B **94**, 121117(R) (2016).
- [39] A. König and N. D. Mermin, *Electronic level degeneracy in nonsymmorphic periodic or aperiodic crystals*, Phys. Rev. B **56**, 13607 (1997).
- [40] S. A. Parameswaran, A. M. Turner, D. P. Arovas, and A. Vishwanath, *Topological order and absence of band insulators at integer filling in non-symmorphic crystals*, Nat. Phys. **9**, 299303 (2013).
- [41] J.-H. Lee, W. Leung, J. Ahn, T. Lee, I.-S. Park, K. Constant, and K.-M. Ho, *Layer-by-layer photonic crystal fabricated by low-temperature atomic layer deposition*, Appl. Phys. Lett. **90**,

- 151101 (2007).
- [42] M. Deubel, G. von Freymann, M. Wegener, S. Pereira, K. Busch, and C. M. Soukoulis, *Direct laser writing of three-dimensional photonic-crystal templates for telecommunications*, Nature Materials **3**, 444-447 (2004).
 - [43] <http://abinitio.mit.edu/wiki/index.php/MITPhotonicBands>.
 - [44] B.-J. Yang, T. Morimoto, and A. Furusaki, *Topological charges of three-dimensional Dirac semimetals with rotation symmetry*, Phys. Rev. B **92**, 165120 (2015).
 - [45] J. Luo, P. Xu, T. Sun, and L. Gao, *Tunable beam splitting and negative refraction in heterostructure with metamaterial*, Appl. Phys. A **104**, 11371142 (2011).
 - [46] S. John and S. Yang, *Electromagnetically Induced Exciton Mobility in a Photonic Band Gap*, Phys. Rev. Lett. **99**, 046801 (2007).
 - [47] K. Ishizaki and S. Noda, *Manipulation of photons at the surface of three-dimensional photonic crystals*, Nature (London) **460**, 367-370 (2009).
 - [48] J. D. Joannopoulos, S. G. Johnson, J. N. Winn, R. D. Meade, *Photonic Crystals: Molding the Flow of Light*, (Princeton University Press, 2008).
 - [49] L. Fu, *Topological crystalline insulators*, Phys. Rev. Lett. **106**, 106802 (2011).
 - [50] L. Fu and C. L. Kane, *Topology, delocalization via average symmetry and the symplectic Anderson transition*, Phys. Rev. Lett. **109**, 246605 (2012).

Acknowledgments

General

We thank Sajeev John, Zhengyou Liu, Ling Lu, Chen Fang, Huanyang Chen, Yun Lai, Chunying Qiu, and Jie Luo for many inspiring discussions.

Funding

H.X.W and J.H.J acknowledge supports from the National Science Foundation of China (Grant no. 11675116) and the Soochow university. Z.H.H is supported by National Science Foundation of China (Grant no. 11574226). Y.C and H.Y.K are supported by NSERC of Canada and Center for Quantum Materials at the University of Toronto.

Author Contributions

J.H.J conceived the idea and wrote the manuscript. H.X.W performed the calculations. H.X.W, Y.C, H.Y.K and J.H.J did the theoretical analysis. J.H.J and H.Y.K guided the research. All authors contributed to uncovering the underlying physics and applications.

Competing interests

The authors declare no competing financial interests.

Data and materials availability

All data needed to evaluate the conclusions in the paper are present in the paper and/or the Supplementary Materials. Additional data related to this paper may be requested from the authors.

Figures

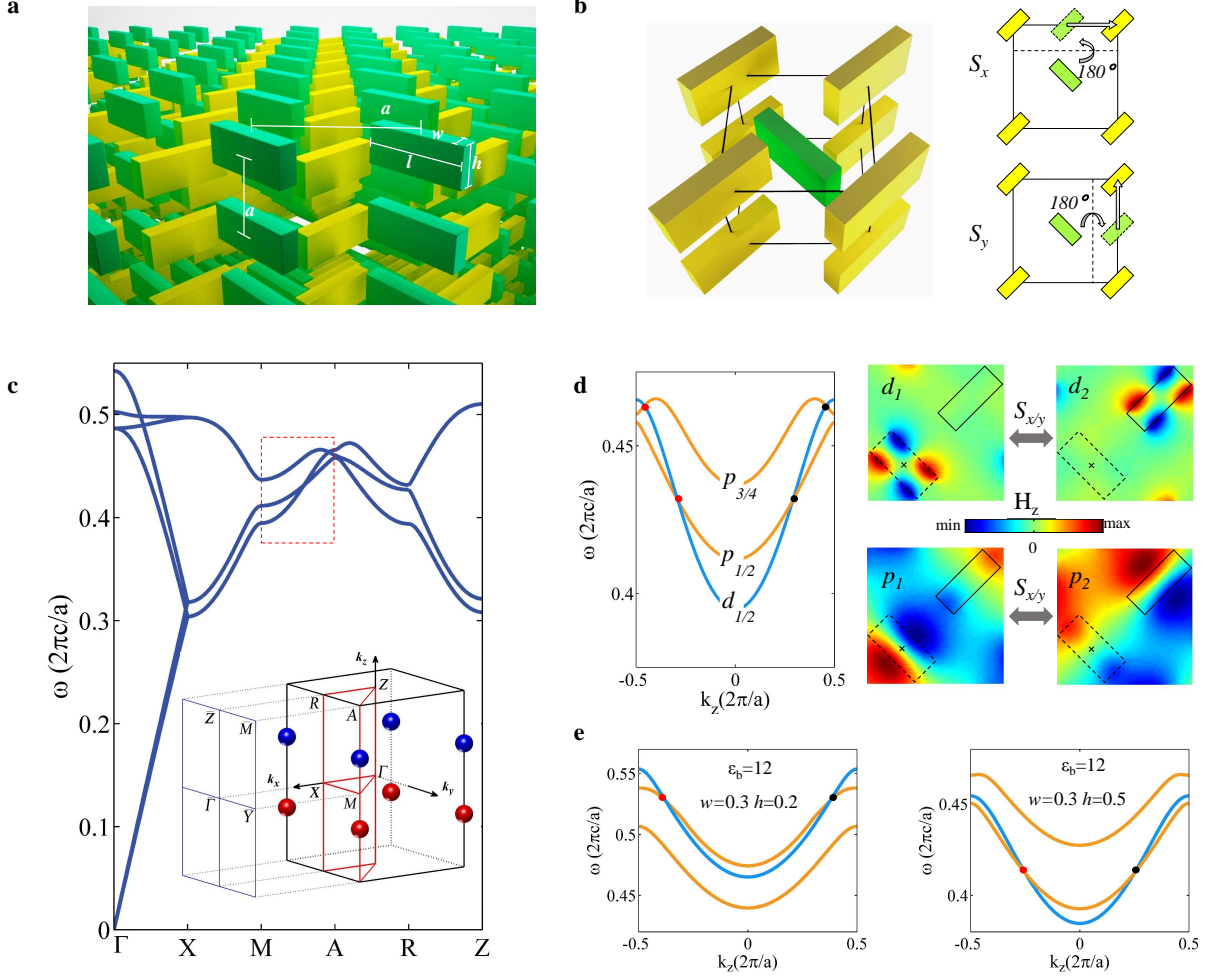


FIG. 1. **All-dielectric photonic-crystals for Dirac points.** **a**, 3D view of the PhC. The yellow and green blocks are of the same material and shape, but positioned and oriented differently. **b**, Left: 3D structure of a unit cell (boundaries are indicated by black lines). Right: Illustration of the two orthogonal screw symmetries S_x and S_y in top-down view. **c**, Photonic band structure. Inset: bulk and surface BZs. The $k_x = \pi$ plane (i.e., X-M-A-R) is doubly degenerate due to the screw symmetry S_x . **d**, Left: Parity inversion on the MA line. Right: magnetic field profiles of the p - and d -wave doublets, respectively. The doubly degenerate states are connected by the screw symmetries, S_x or S_y . Parameters $l = 0.5a$, $w = 0.2a$, $h = 0.5a$, and permittivities $\epsilon_b = 16$ and $\epsilon_m = 1.9$. **e**, Band inversion for other substantially different parameters. DPs of topological charge $\mathcal{N}_{DP} = +1, -1$ are labeled as red and blue (red and black) in **c** (**e**), separately. Frequencies are in unit of $2\pi c/a$ with c being the speed of light in vacuum.

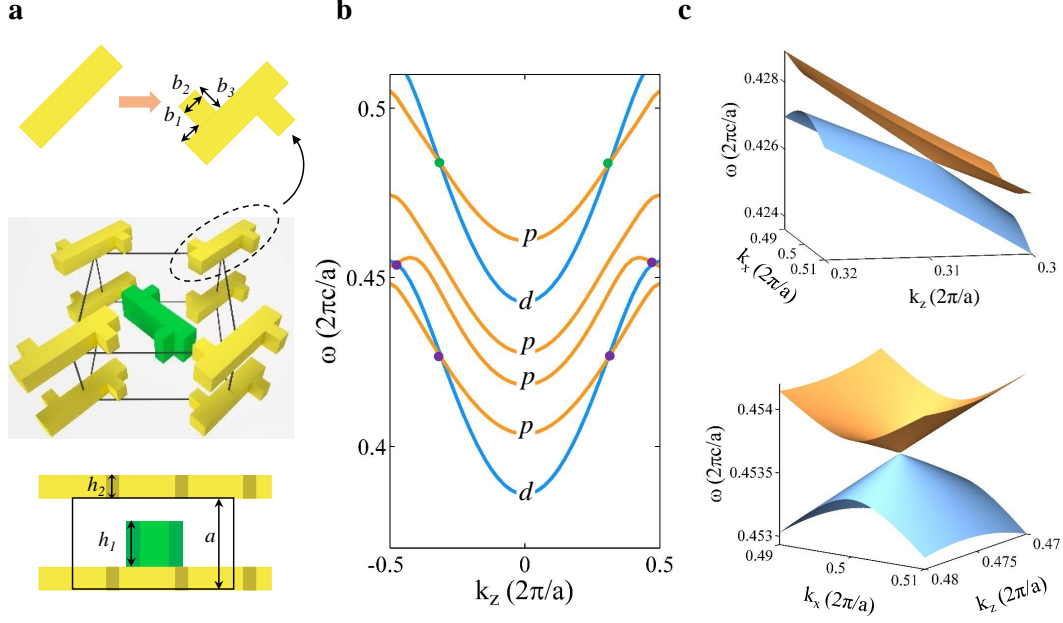


FIG. 2. **Weyl points derived from Dirac points.** **a**, Unit-cell structure of the symmetry-broken PhC. Upper panel: 3D view with zoom-in illustration of structure deformations. Lower panel: side view from $[1\bar{1}0]$ direction. The geometry parameters are $b_1 = 0.1$, $b_2 = 0.11$, $b_3 = 0.094$, $h_1 = 0.5$, and $h_2 = 0.3$. The z coordinates of the centers of the two types of dielectric blocks are 0 and $0.65a$, respectively. **b**, Band structure on the MA line for part of the first six photonic bands indicates removal of double degeneracy and linear-crossing between non-degenerate p - and d -states. These crossings are identified as type-I and type-II WPs. Purple (green) dots stand for WPs with Chern number -1 (+1). **c**, Dispersions of a type-II WP (upper panel) and a type-I WP (lower panel). The former is due to the crossing between band 1 and 2, while the latter originates from the crossing between band 1 and 3. The bands are numerated in ascending order at the M point.

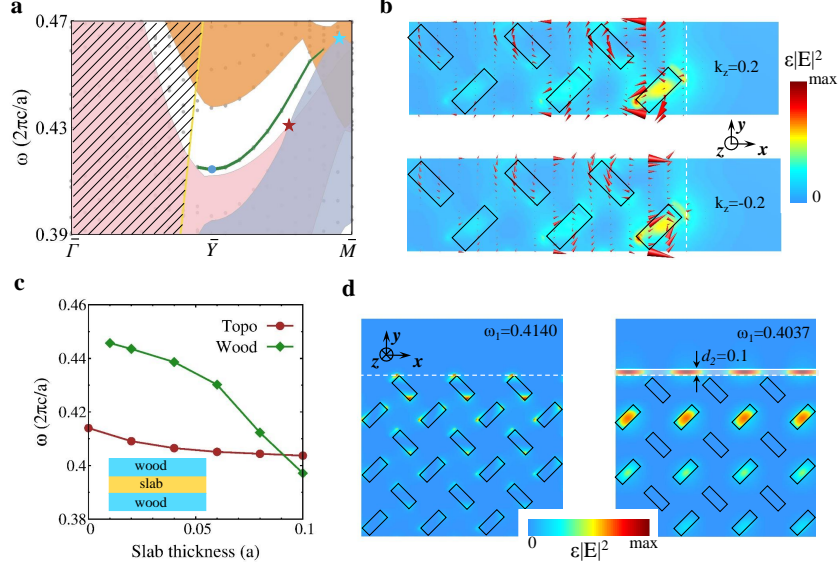


FIG. 3. **Dirac points and topological surface states.** **a**, Surface band and projected bulk bands on (100) PhC-air interface. The blue (brown) star represents a type-I (type-II) DP, which are the crossing point of band 1,2 (gray region) and band 5,6 (brown region) [band 3,4 (pink region)]. The surface band (green curve) is below the light-line (the golden line). The region above the light-line is depicted by the shadow. Gray dots represent the spectrum from a finite-size supercell calculation (see Methods). **b**, Energy density and Poynting vector profiles for the topological surface states at two opposite wavevectors with $k_y = \pi$. **c**, Stability of the topological (“Topo”) surface states. Frequency of the topological surface state at \bar{Y} vs. thickness of a slab with permittivity $\epsilon = 8$ on top of the PhC surface. The reference curve is the same dependence for the slab-defect state induced by a slab of the same permittivity embedded in a woodpile (“Wood”) PhC (structure schematically shown in the inset). **d**, Field energy distribution of the topological surface states at \bar{Y} point for slab thickness 0 (Left) and $0.1a$ (Right), respectively.

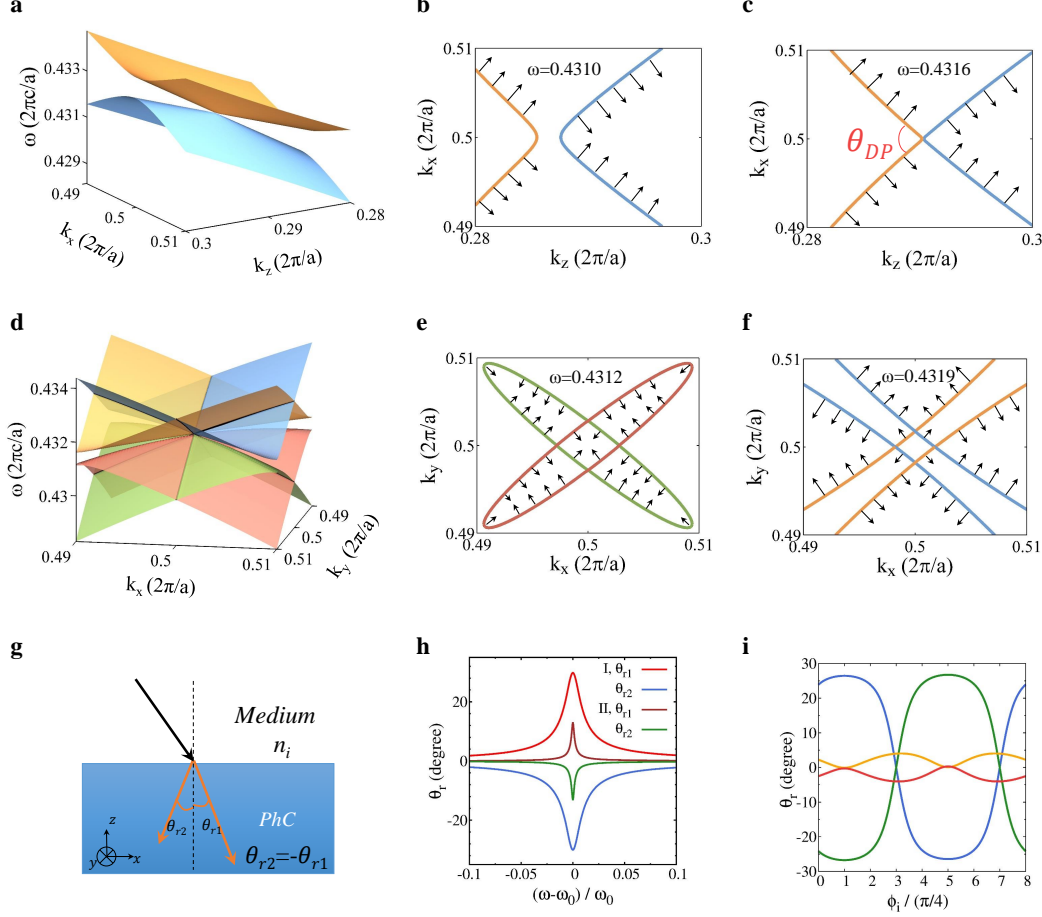


FIG. 4. **Type-II Dirac cone and anomalous refraction.** **a**, Type-II Dirac dispersion on the k_x - k_z plane. **b**, Isofrequency contours (orange and blue curves for the upper and lower branches, respectively) and group velocities (black arrows) on the k_x - k_z plane for a frequency below the type-II DP. **c**, Similar to **b**, but for the frequency at the DP. **d**, Dispersion of the Dirac cone on the k_x - k_y plane. **e** and **f**, Isofrequency contours on the k_x - k_y plane for frequencies below and above the DP, respectively. **g**, Schematic of anomalous refraction of type-II DPs: simultaneous positive and negative refraction with opposite refraction angles. **h**, Refraction angles vs. frequency for two cases with $\phi_i = 0$. Case I: $\gamma = 1$ and $q_{\parallel} = 0.2\frac{\pi}{a}$. Case II: $\gamma = 0.4$ and $q_{\parallel} = 0.1\frac{\pi}{a}$. **i**, Refraction angles vs. angle ϕ_i for $\gamma = 1$ and $q_{\parallel} = 0.1\frac{\pi}{a}$ and $\frac{\delta\omega}{\omega_0} = 0.005$ with $\omega_0 = 0.4\frac{2\pi c}{a}$.

Supplementary Materials

Sec. SI Other symmetries and their consequences

In addition to the symmetries listed in the main text, there are also two glide symmetries, $G_x \equiv S_x * \mathcal{P}$ and $G_y \equiv S_y * \mathcal{P}$, which are irrelevant to the Dirac points and Weyl points studied in this work. Nevertheless these two glide symmetries can lead to Kramers double degeneracy on several high symmetry lines: the RZ line ($k_y = 0, k_z = \pi$) and the MY line ($k_y = \pi, k_z = 0$) (as shown in Fig. 1c in the main text). This is because $G_x * \mathcal{T}$ is an invariant operator on both these lines and $(G_x * \mathcal{T})^2 = T_{011} = -1$ for both lines.

Sec. SII Robustness of Kramers degeneracy and parity inversion through screw symmetries

Here we show that the realization of Kramers degeneracy and the emergence of parity inversion are robust to the material and geometry of the photonic crystals (PhCs). We calculate the photonic bands for the $k_x = \pi$ plane with four different geometric/material parameter sets. The results of the photonic bands are shown in Figure S1 where we also show the parity inversion on the MA line. We find that the synthetic Kramers double degeneracy on the $k_x = \pi$ plane holds for all parameters. This is because such double degeneracy are guaranteed by the screw symmetry S_x . In addition, the parity of the photonic bands are well-defined on the MA line. For all four sets of parameters in Figure S1, we observe parity inversion and emergence of DPs in the first six photonic bands. In these parameters, we adopted the permittivity of the blocks as $\varepsilon_b = 12$ (silicon) or 10 (e.g., GaAs) and the permittivity of the background medium as $\varepsilon_m = 2$ (polymer). The geometric parameters of the blocks are also varied. The robustness of the method on the realization of Dirac points on the MA line is thus robust to material parameters. This also indicates the stableness of the Dirac points and implies that such a symmetry-guided method can also be effective in other classical/bosonic systems.

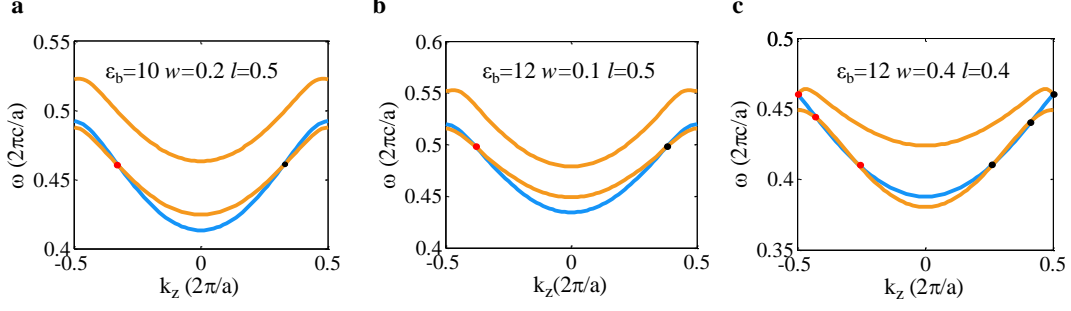


Figure S1: Photonic bands on the MA line for various geometry/material

parameters. **a**, Permittivity of the blocks $\varepsilon_b = 10$ (e.g., GaAs), the width of the blocks $w = 0.2$, and the height of the blocks $h = 0.5$. **b**, $\varepsilon_b = 12$ (silicon), $w = 0.1$, and $h = 0.5$. **c**, $\varepsilon_b = 12$, $w = 0.3$, and $h = 0.2$. **d**, $\varepsilon_b = 12$, $w = 0.3$, and $h = 0.5$. The figures show the first six bands of different parities (red: odd-parity, blue: even-parity) on the MA line. A crossing between bands of different color gives a Dirac point. Common parameters: permittivity of the background medium $\varepsilon_m = 2$ (polymer) and the length of the blocks $l = 0.5$.

Sec. SIII $\vec{k} \cdot \vec{P}$ theory for the Dirac points

Around a Dirac point, there are four states interacting with each other. According to the field profiles shown in Figure S3 in the main text, there are two p -wave states of which the spatial symmetry coincide with x_1 and x_2 where $x_1 = (x+y)/\sqrt{2}$ and $x_2 = (-x+y)/\sqrt{2}$. We shall denote them as $|p_1\rangle$ and $|p_2\rangle$, respectively. The other two states are d -waves which have the same spatial symmetry as x_1x_2 and $x_1x_2(x_1^2 - x_2^2)$, respectively. They shall be labeled as $|d_1\rangle$ and $|d_2\rangle$, respectively. According to the field profiles, we observe that $\langle p_i | S_x | p_i \rangle = 0$ for $i = 1, 2$, and $\langle p_1 | S_x | p_2 \rangle = -i = -\langle p_2 | S_x | p_1 \rangle$. Thus S_x is manifested as σ_y between the two degenerate p -states. This is also true for the d -states: $\langle d_i | S_x | d_i \rangle = 0$ for $i = 1, 2$, and $\langle d_1 | S_x | d_2 \rangle = -i = -\langle d_2 | S_x | d_1 \rangle$. The Θ_x operation is then simply $\Theta_x = \sigma_y \mathcal{K}$ where \mathcal{K} is complex conjugation. Here the Pauli matrices σ_i ($i = x, y, z$) act on the “spin” space within each doublet of a given parity. The Kramers degeneracy is due to $\Theta_x^2 = -1$. A better choice of “spin” is to construct the four states as $|p_{\pm}\rangle = \frac{1}{\sqrt{2}}(|p_1\rangle \pm i|p_2\rangle)$ and $|d_{\pm}\rangle = \frac{1}{\sqrt{2}}(|d_1\rangle \pm i|d_2\rangle)$. These four states carry total angular momentum (see Figure S2) which can be leveraged to emulate “spin”. Though we will eventually switch to such a representation, we stay for the p_1, p_2, d_1 and d_2 basis for now for simplicity.

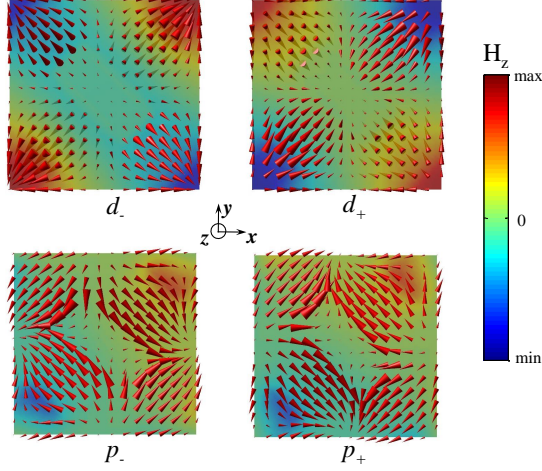


Figure S2: Magnetic field H_z and Poynting vector profiles of the d_{\pm} and p_{\pm} states at a slice of the unit cell. Profiles on this slice (with a fixed z coordinate) indicate that the Poynting vectors have a nontrivial winding approximately along the z axis. Such winding indicates that these states carry finite total angular momenta along the z direction. The opposite winding between p_+ and p_- (d_+ and d_-) states reflects that they carry opposite total angular momenta.

The aim of this section is to construct a $\vec{k} \cdot \vec{P}$ theory for the Dirac points to understand the dispersions around the Dirac points, particularly in the k_x - k_y plane. The photonic bands are solutions of the following eigenvalue equations

$$\nabla \times \frac{1}{\varepsilon(\vec{r})} \nabla \times \vec{h}_{n,\vec{k}}(\vec{r}) = \frac{\omega_{n,\vec{k}}^2}{c^2} \vec{h}_{n,\vec{k}}(\vec{r}), \quad (13)$$

where n is the band index and $\vec{h}_{n,\vec{k}}(\vec{r})$ is the Bloch function for the magnetic field of the electromagnetic wave. It is normalized as $\int_{u.c.} d\vec{r} \vec{h}_{n',\vec{k}}^*(\vec{r}) \vec{h}_{n,\vec{k}}(\vec{r}) = \delta_{nn'}$ with $u.c.$ denoting the unit cell (i.e., integration within a unit cell). The Hermitian operator $\nabla \times \frac{1}{\varepsilon(\vec{r})} \nabla \times$ is then regarded as the “photonic Hamiltonian” [32].

The $\vec{k} \cdot \vec{P}$ theory is constructed by expanding the Bloch functions of photonic bands near the DP with the Bloch functions at the DP. Direct calculation yields, the following $\vec{k} \cdot \vec{P}$ Hamiltonian,

$$\mathcal{H}_{nn'}(\vec{k}) = \frac{\omega_{n,0}^2}{c^2} \delta_{nn'} + \vec{q} \cdot \vec{P}_{nn'} - \int_{u.c.} \frac{d\vec{r}}{\varepsilon(\vec{r})} \vec{h}_{n,0}^*(\vec{r}) \cdot [\vec{q} \times (\vec{q} \times \vec{h}_{n',0}(\vec{r}))], \quad (14)$$

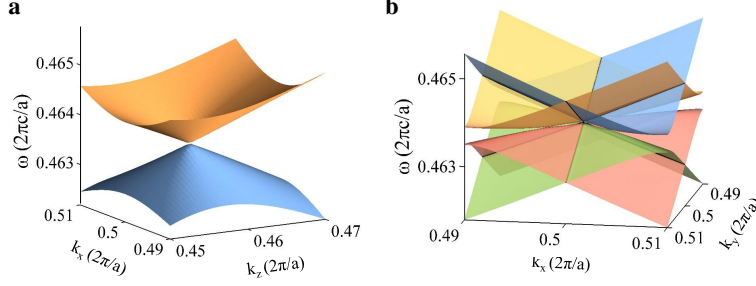


Figure S3: Dispersion of the type-I Dirac points. 3D dispersion of the type-I Dirac point at $k_z > 0$ for $h = 0.5$, $w = 0.2$, $l = 0.5$, $\varepsilon_b = 16$, and $\varepsilon_m = 1.9$. **a**, Dispersion on the k_z - k_x plane. **b**, Dispersion on the k_x - k_y plane around the DP.

where $\omega_{n,0}$ is the eigen-frequency of the n^{th} band at the DP. The matrix element of \vec{P} is given by

$$\vec{P}_{nn'} = \int_{u.c.} \frac{d\vec{r}}{\varepsilon(\vec{r})} [\vec{h}_{n',0}(\vec{r}) \times (i\nabla \times \vec{h}_{n,0}^*(\vec{r})) + (i\nabla \times \vec{h}_{n',0}(\vec{r})) \times \vec{h}_{n,0}^*(\vec{r})]. \quad (15)$$

A crucial fact is that the matrix element $\vec{P}_{nn'}$ is nonzero only when the n and n' bands are of different parity. In our system the mirror planes are the (110) and (1 $\bar{1}$ 0) planes. Therefore, we shall calculate the two momentum matrix elements, $\hat{P}_1 = (\hat{P}_x + \hat{P}_y)/\sqrt{2}$ and $\hat{P}_2 = (-\hat{P}_x + \hat{P}_y)/\sqrt{2}$. According to the symmetry of the p and d states, we find that \vec{q} -linear terms in the basis of $(|d_1\rangle, |d_2\rangle, |p_1\rangle, |p_2\rangle)^T$ is

$$q_1 P_1 + q_2 P_2 = \begin{pmatrix} 0 & 0 & a_1 q_2 & a_2 q_1 \\ 0 & 0 & b_1 q_2 & b_2 q_1 \\ a_1^* q_2 & b_1^* q_2 & 0 & 0 \\ a_2^* q_1 & b_2^* q_1 & 0 & 0 \end{pmatrix},$$

$$q_z P_z = \frac{2\omega_0 v}{c^2} (q_z \tau_z + \eta q_z \tau_0), \quad (16)$$

where ω_0 is the frequency of the Dirac point, v is the group velocity along the z direction, η measures the deformation of the Dirac cone along the z direction. The Pauli matrix τ_i ($i = 0, z$) is defined in such a way that τ_z gives the parity of the photonic states. Here we consider the Dirac point with $k_z > 0$.

The invariance of the Hamiltonian under Θ_x implies that

$$\Theta_x \mathcal{H}(\vec{k}) \Theta_x^{-1} = \mathcal{H}(\Theta_x \vec{k}) \quad (17)$$

Note that $\Theta_x \vec{k} = S_x \mathcal{T} \vec{k} = -S_x \vec{k} = (-k_x, k_y, k_z)$. Because $q_1 = (k_x + k_y)/\sqrt{2}$ and $q_2 = (-k_x + k_y)/\sqrt{2}$, we find $\Theta_x q_1 = q_2$ and $\Theta_x q_2 = q_1$. We thus find that

$$a_1 = -b_2^*, \quad a_2 = b_1^*. \quad (18)$$

We then define $\alpha \equiv \frac{c^2}{2\omega_0 v} a_1$ and $\beta \equiv \frac{c^2}{2\omega_0 v} a_2$ and find

$$q_1 P_1 + q_2 P_2 = \frac{2\omega_0 v}{c^2} \begin{pmatrix} 0 & 0 & \alpha q_2 & \beta q_2 \\ 0 & 0 & \beta^* q_1 & -\alpha^* q_1 \\ \alpha^* q_2 & \beta q_1 & 0 & 0 \\ \beta^* q_2 & -\alpha q_1 & 0 & 0 \end{pmatrix}. \quad (19)$$

Up to the \vec{q} linear order, the Hamiltonian \mathcal{H} gives a spectrum without degeneracy, except for $q_1 = \pm q_2$ (i.e., on the $k_x = \pi$ and $k_y = \pi$ planes). Therefore, the spectrum in the k_x - k_y plane has four branches for a generic direction. Only for the $q_1 = \pm q_2$ case the spectrum is double degenerate and has only two branches. Physically, the double degeneracy on the $k_x = \pi$ and $k_y = \pi$ planes is induced by the screw symmetries S_x and S_y . Specific dispersions around the type-I and type-II Dirac points on the k_x - k_y plane is shown in Figure S3b in the Supplementary Materials and Fig. 2b in the main text, respectively.

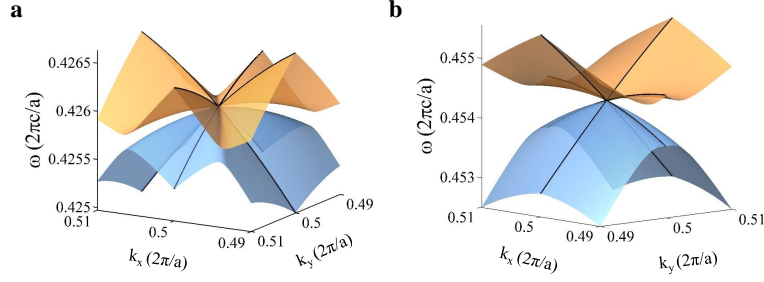


Figure S4: Dispersion of Weyl points on the k_x - k_y plane. **a**, 3D dispersion around the first type-II Weyl point at $k_z > 0$ on the k_x - k_y plane. **b**, 3D photonic spectrum around the first type-I Weyl point at $k_z > 0$.

Sec. SIV Weyl points on MA line for symmetry-broken photonic crystals

The photonic spectra of type-I and type-II Weyl points on the k_x - k_y plane around the Weyl points are shown in Figure S4, confirming the linear dispersion around the Weyl point on the k_x - k_y plane.

The distributions of the magnetic field H_z for the first six photonic bands on the MA line are shown in Fig. 3. The spatial distributions of H_z indicates two kinds of states: odd-parity states and even-parity states. All the odd-parity states are of p -wave nature, while all the even-parity states are of d -wave nature. There are four p -wave bands and two d -wave bands.

Due to the chiral structure, the photonic bands carry angular momenta. This is indicated by the rotation of the Poynting vector in each unit cell. According to such rotations, we can label the d state with angular momentum along z direction as d_+ , while the d state with opposite angular momentum as d_- . Similarly for the p -waves, we have p_+ and p_- states. According to the $\vec{k} \cdot \vec{P}$ analysis in Ref. [32], only the crossings between p_- and d_- or between p_+ and d_+ can lead to Weyl points, whereas the coupling between p_+ and d_- and other combinations cannot lead to \vec{k} -linear spectrum with nonzero Chern number. In our PhCs, counting in frequency-ascending order, the first Weyl point is due to the crossing between the p_- and d_- state, as indicated by the field profiles near the Weyl point. The second Weyl point is due to the crossing between another p_- state and the d_- state. The third Weyl point is due to the crossing between the p_+ and d_+ states.

We shall now apply the $\vec{k} \cdot \vec{P}$ theory to show that the crossing between p_- and d_- states

at $k_z > 0$ leads to a Weyl point with Chern number -1. The two states can be represented according to their spatial symmetry as

$$|p_-\rangle = |c_1x - ic_2y\rangle, \quad |d_-\rangle = |f_1(x^2 - y^2) - 2if_2xy\rangle. \quad (20)$$

The coefficients $c_i > 0$ and $d_i > 0$ ($i = 1, 2$) characterizes the anisotropy of the p_- and d_- states, which can be determined numerically via the field distributions from ab initio simulation. However, the analysis here is already sufficient to determine the Chern number of the Weyl points, which is a topological quantity that does not depend on the specific numbers of the coefficients. The $\vec{k} \cdot \vec{P}$ Hamiltonian between the two states in the basis of $(|d_-\rangle, |p_-\rangle)^T$ is then

$$\begin{aligned} \mathcal{H} &= q_x P_x + q_y P_y + q_z P_z, \\ q_x P_x + q_y P_y &= \mathcal{B}[(c_1 f_1 + c_2 f_2) q_x \sigma_x - i(c_1 f_2 + c_2 f_1) q_y \sigma_y], \\ q_z P_z &= \frac{2\omega'_0 v'}{c^2} (q_z \sigma_z + \eta' q_z \sigma_0), \end{aligned} \quad (21)$$

where $\mathcal{B} = \langle x | i\partial_x | (x^2 - y^2) \rangle = -\langle y | i\partial_y | (x^2 - y^2) \rangle = \langle x | i\partial_y | 2xy \rangle = \langle y | i\partial_x | 2xy \rangle$ is the $\vec{k} \cdot \vec{P}$ coefficient and can be set as a real number via a universal $U(1)$ transformation, ω'_0 is the frequency of the Weyl point and the coefficient η' describes the deformation of the Weyl point along the k_z direction. σ_i ($i = x, y, z$) are the Pauli matrices, and σ_0 is the 2×2 identity matrix. The above Hamiltonian gives a Weyl point with Chern number $-\text{sgn}(v')$. For the photonic spectrum given in Fig. 5 in the main text, $v' > 0$, and the Chern number is thus -1 .

In the $k_z < 0$ region, there is another Weyl point linked by time-reversal operation, which is hence a crossing between the $|p_+\rangle$ and $|d_+\rangle$ states. This Weyl point has Chern number $\text{sgn}(v')$. However, the velocity also switches sign, leading to a Chern number of -1 , as well. The crossing between the $|p_+\rangle$ and $|d_+\rangle$ states in the $k_z > 0$ region is then a Weyl point with a Chern number of $+1$. The time-reversal partner of this Weyl point also has Chern number of $+1$.

Sec. SV Disorder effects

We now study the effects of disorder on the DPs and topological surface band. We shall use crude spatial meshes in the photonic spectrum calculation to mimic disorders. Crude spatial meshes roughen the surface of the dielectric blocks, introducing surface imperfection (see the

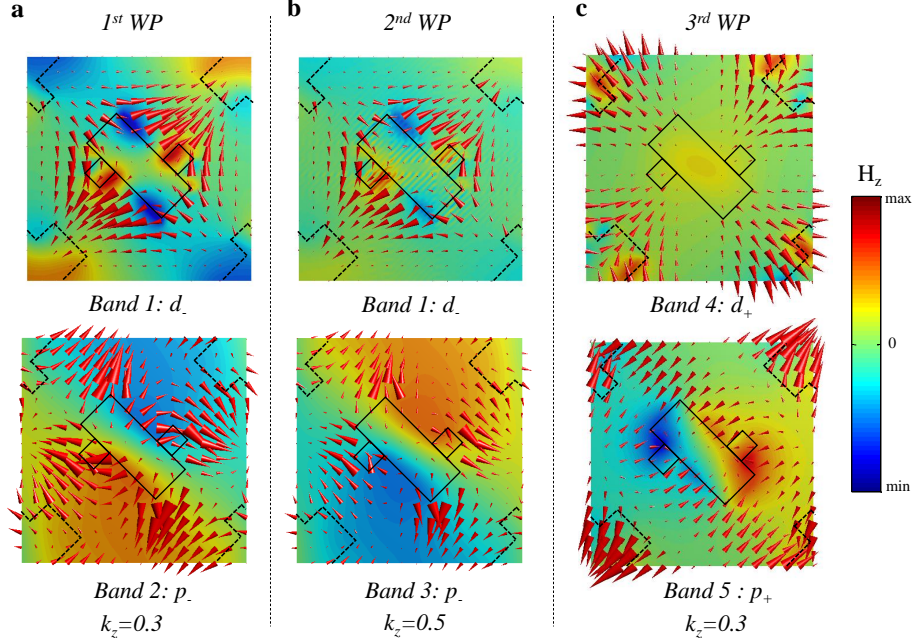


Figure S5: Field profiles of the upper and lower branches of the first three Weyl points with $k_z > 0$. **a—c:** Distributions of the magnetic field H_z (real part) for the first, second, and third WP, separately. Upper panels: the lower branch of each WP, lower panels: the upper branch of each WP. The Poynting vectors (red arrows, only the x - y plane components are indicated in the figures) have rotating distributions around the unit cell center, which indicates finite angular momentum along the z direction. According to their angular momenta, these bands can be labeled as p_+ or d_+ states (if the angular momentum is along z direction), or p_- or d_- state (if the angular momentum is along the $-z$ direction).

inset of Figure S6a). The surface roughness is on the scale of a/N where N is the number of mesh points along x , y or z direction. At very small N (such as $N = 8$ as illustrated in the inset of Figure S6a) the roughness not only affect the surface but also the inside of the dielectric blocks. We check numerically whether such strong disorder effects can affect the DPs and the topological surface band.

Exactly speaking, with these disorders, the fourfold degeneracy of the DPs are lifted. Splitting of degeneracy is quantified by $\Delta\omega_0/\omega_0$ where $\Delta\omega_0$ is the largest frequency minus the smallest frequency of the four nearly degenerate bands, and ω_0 is the averaged frequency. It is shown in Figure S6a that such splitting is negligibly small even for very low resolution $N = 8$. The manifested robustness of the DPs against disorders is even more pronounced

than the DPs stabilized by the point group symmetry as studied in Ref. [32]. We also study the robustness of the topological surface states against disorders using a similar approach: reducing the spatial resolution in the calculation. In Figure S6b, we show that the modification of the frequency of the topological surface state on \bar{Y} is also very small (smaller than 2%) for a resolution as small as $N = 8$. The frequency change $\Delta\omega_{\bar{Y}}$ here is defined as the frequency of the surface state at \bar{Y} for a smaller resolution minus that for the very large resolution $N = 64$. Therefore, we have shown that both the DPs and the topological surface states are robust against disorders.

Sec. SVI Refraction angles for generic \vec{q}

To consider the refraction angles for generic \vec{q} (i.e., away from the x - z or y - z plane), we shall consider the following dispersion

$$\omega = \omega_0 + v(\eta q_z + \rho \sqrt{\gamma^2 q_\tau^2 + q_z^2}) + \gamma' \frac{v^2(q_1^2 + q_2^2)}{\omega_0}, \quad \rho = \pm 1, \quad \tau = 1, 2. \quad (22)$$

Here $q_1 = \frac{q_x + q_y}{\sqrt{2}}$ and $q_2 = \frac{-q_x + q_y}{\sqrt{2}}$. The dimensionless constant γ' determines the quadratic dispersion which is important for \vec{q} along the q_1 or q_2 direction. The displacement of wavevector from the DP $\vec{q} = \vec{k} - \vec{K}_0$ [$\vec{K}_0 = (\frac{\pi}{a}, \frac{\pi}{a}, k_0)$] is determined by

$$q_x = q_{\parallel} \cos(\phi_i), \quad q_y = q_{\parallel} \sin(\phi_i). \quad (23)$$

The parameter q_{\parallel} is fixed, but the angle ϕ_i is varied. Other parameters are also taken from the photonic band calculation, e.g., $v \simeq 0.02c$, $\omega_0 \simeq 0.4 \frac{2\pi c}{a}$, $\eta \simeq -2$, $\gamma \simeq 1$ and $\gamma' \simeq -0.5$. $q_{\parallel} = 0.05 \frac{2\pi}{a}$ or $0.1 \frac{2\pi}{a}$.

We now define

$$\delta = \frac{1}{v}(\omega - \omega_0 - \gamma' \frac{v^2(q_1^2 + q_2^2)}{\omega_0}). \quad (24)$$

One then finds

$$(\delta - \eta q_z)^2 = \gamma^2 q_\tau^2 + q_z^2. \quad (25)$$

Here $q_1 = (q_x + q_y)/\sqrt{2}$ and $q_2 = (-q_x + q_y)/\sqrt{2}$ which vary with the angle ϕ_i according to Eq. (23). However, the wavevector perpendicular to the interface, q_z , is not conserved. q_z is in fact determined by the solutions of the above equation. We find that

$$q_z^{\pm, \tau} = \frac{\eta \delta \pm \sqrt{\eta^2 \delta^2 - (\eta^2 - 1)(\delta^2 - \gamma^2 q_\tau^2)}}{\eta^2 - 1}, \quad \tau = 1, 2. \quad (26)$$

For $\eta < -1$ ($\eta > 1$) the isofrequency contour always give larger q_z for the upper (smaller) branch (a case with $\eta > 1$ is shown in Figs. 2b and 2c in the main text). Therefore, q_z^ρ is the solution for the ρ branch. There are four solutions since there are four nondegenerate bands that intersect with the isofrequency plane. The group velocity is given by

$$v_1|_{\tau=1} = \left. \frac{\partial \omega}{\partial q_1} \right|_{\tau=1} = \rho v \frac{\gamma^2 q_1}{\sqrt{\gamma^2 q_1^2 + q_z^2}} + \frac{2\gamma' v^2 q_1}{\omega_0}, \quad (27a)$$

$$v_2|_{\tau=1} = \left. \frac{\partial \omega}{\partial q_2} \right|_{\tau=1} = \frac{2\gamma' v^2 q_2}{\omega_0}, \quad (27b)$$

$$v_z|_{\tau=1} = \left. \frac{\partial \omega}{\partial q_z} \right|_{\tau=1} = v \left(\eta \pm \frac{q_z}{\sqrt{\gamma^2 q_1^2 + q_z^2}} \right). \quad (27c)$$

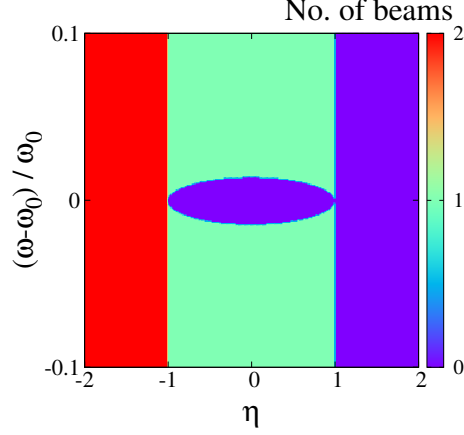


Figure S6: Number of refraction beams as a function of η and frequency. There are two refraction beams for $\eta < -1$, whereas there is no refraction beam for $\eta > 1$. For $|\eta| \leq 1$ the number of refraction beams depends on the frequency and the parameter η .

For light injected from the medium above the PhC only beams with $v_z < 0$ yield refraction. Therefore, for $\eta > 2$, there is no solution, for $|\eta| < 1$ there is one solution, for $\eta < -2$, there are two solutions (see Figure S6).

For the $\tau = 2$ branches, we have

$$v_1|_{\tau=2} = \frac{2\gamma'v^2q_1}{\omega_0}, \quad (28a)$$

$$v_2|_{\tau=2} = \rho v \frac{\gamma^2 q_2}{\sqrt{\gamma^2 q_2^2 + q_z^2}} + \frac{2\gamma'v^2 q_2}{\omega_0}, \quad (28b)$$

$$v_z|_{\tau=2} = v \left(\eta \pm \frac{q_z}{\sqrt{\gamma^2 q_2^2 + q_z^2}} \right). \quad (28c)$$

The refraction angles are obtained as

$$\theta_r = -\arctan\left(\frac{v_{\parallel}}{v_z}\right) \quad (29)$$

where v_{\parallel} is the projection of the group velocity on the parallel wavevector direction,

$$v_{\parallel} = \vec{v} \cdot \vec{e}_{k_{\parallel}}, \quad \vec{e}_{k_{\parallel}} = \frac{1}{\sqrt{k_x^2 + k_y^2}}(k_x, k_y, 0), \quad k_i = \pi + q_i, \quad (i = x, y). \quad (30)$$

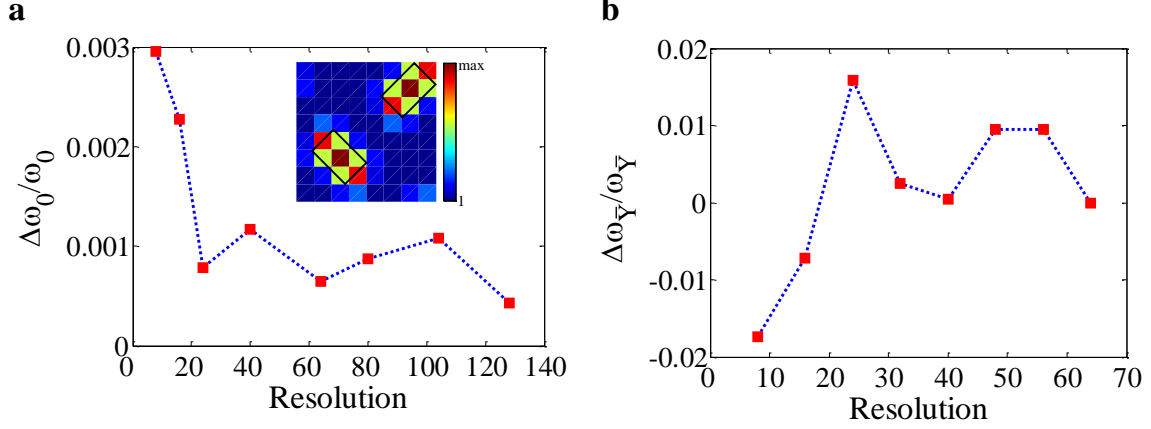


Figure S6: Robustness of the Dirac points and surface states against disorders. **a**, The ratio of the frequency splitting of the type-II DP $\Delta\omega_0$ over the frequency of the type-II DP ω_0 vs. the spatial resolution. Inset: The structure of the dielectric blocks at a low spatial resolution with crude meshes ($N = 8$); The black boxes indicate the ideal shape and position of the two dielectric blocks; The color bar indicate the permittivity with maximum value close to $\varepsilon_b = 16$. **b**, The ratio of the change of the frequency of the topological surface state at \bar{Y} , $\Delta\omega_{\bar{Y}}$, over the frequency of the topological surface state $\omega_{\bar{Y}}$ at $N = 64$, as a function of the spatial resolution.